Biointerface Research in Applied Chemistry
Open-Access Journal (ISSN: 2069-5837)

Article
Volume 16, Issue 1, 2026, 38
https://doi.org/10.33263/BRIAC161.038

In Situ Measuring of Bio-Composites for Predicting Explosion in LIBs: A Resistance and Temperature Sensor

Majid Monajjemi [1,*], Fatemeh Mollaamin [2], Amirhosein Mojri [3], Zahra Solati [3], Melika Aghaei [3]

[1] Department of Biology, Faculty of Science, Kastamonu University, Kastamonu, Turkey
[2] Department of Biomedical Engineering, Faculty of Engineering and Architecture, Kastamonu University, Kastamonu, Turkey
[3] Department of Chemical Engineering, CT.C., Islamic Azad University, Tehran, Iran
* Correspondence: maj.monajjemi@iauctb.ac.ir;

Received: 2.10.2025; Accepted: 18.11.2026; Published: 15.02.2026

Abstract: Nickel-rich cathode materials, due to their high operating voltage and superior energy density, are needed for ever-increasing EV mileage for any novel technologies in wider worlds. However, to date, their efficiency and use are not widespread due to challenges related to structural instability, limited thermal safety, and suboptimal cycle life relative to the ideal target. In this work, we designed and manufactured a temperature-monitoring sensor, including engineering strategies to enhance cathode performance using a mechanical hydrogen sensor for early safety warnings in electric vehicles. Since the generation of H_2 from the reaction of lithium metal with polymers occurs before the "thermal runaway", detection of hydrogen, even at negligible levels, by a sensor can serve as a warning. In this work, we investigated sensing mechanisms of the H_2 sensor through the resistive RT H_2 sensors for early safety warning of LIBs. We also used advanced Techniques for Internal temperature monitoring in our fabricated sensor. In this work, we synthesized six Ni-rich cathode materials as composites via the gel method, using in situ design and manufacturing, and tested a temperature-monitoring sensor. We found a composite with a structure of $LiNi_{0.778}Ti_{0.111}Co_{0.111}PO_4$ containing faulty voltage 0.51-0.59 and detection time of (R2C=31000) seconds, as well as capacity (Ah) range between 16.12-18.95 and faulty amperage detection (A) between 1.15-3.75, which has the most efficiency and safety warning for electric vehicle usage compared with other samples in Ni-rich cathode materials.

Keywords: mechanical hydrogen sensor; Ni-rich lithium-ion batteries; safety warning in electric vehicles; increasing EV mileage.

1. Introduction

Since lithium-ion batteries (LIBs) are mostly used for energy storage in electric vehicles (EVs), they fall short of meeting the demand for large EV mileage, and require LIBs with high energy density. Obviously, this energy can be provided by the high-quality cathode materials, and any more redox potential of this material vs. Li/Li^+ could produce the highest energy density. In past decades, the first commercial fabrication of $LiNi_{1/3}Mn_{1/3}Co_{1/3}O_2$ (NMC333) was successful for NMC-based cathode materials in laboratories and factories. In this composition, Ni appears as an active element through $Ni^{2+/3+}$ and $Ni^{3+/4+}$ redox couples, whereas manganese and cobalt stabilize the layered structure. Consequently, Ni concentration increases instead of cobalt and manganese without destroying the layered structure needed for the electrochemical performance. By this target, Ni-rich $LiNi_{(1-x-y)}Co_xM_yO_2$ (NMC, 1-x-y⩾0.5, M = Mn, Fe, Mg, or Al) {(such as and $LiNi_xCo_yMn_z\ Al_{(1-x-y-z)}\ O_2$ (NCMA)} are a suitable choice for low-cost, high-capacity, and particularly low toxic cathode materials that already used and as well can be designed to fabricate for ever increasing EV mileage in future research [1-8]. An important composition of Ni-rich cathode elements can be fabricated by $LiNi_xCo_yAl_zO_2$ with $x \geq 0.8$ (NCA), which has similar electrochemical behavior to NMC with identical efficiency. Recently, other commercial Ni-rich composite materials, such as $LiNi_{0.8}Mn_{0.1}Co_{0.1}O_2$ (NMC811) and $LiNi_{0.8}Co_{0.15}Al_{0.05}O_2$, with higher energy densities and better thermal stabilities compared with NCA, NCM811 were synthesized. [9-11]. Unfortunately, in higher Ni concentrations of Ni, electrode–electrolyte deterioration [12], micro-crack producing [13], and NiO rock-salt phase appear in mole fraction equal x = 0.8 [14, 15]. So although enhancing Ni concentration increases the capacity, the structure is destroyed due to the reduction of cobalt and manganese concentrations, resulting in the capacity fading and impedance increasing [16,17]. In total, NMC containing more manganese has better cycling stability [18, 19], while NMC with more nickel mole fraction could not reach high voltages due to the lack of Mn^{4+} as a structure stabilizer [20]. From the viewpoint of thermal runaways, the safety issues of Ni-rich NMC and NCA are similar [21], but NCA cells react faster than NMC cells above 1°C min^{-1} [22]. In addition, the high redox potential of Ni-rich cathode materials is also a cause of their poor thermal and structural stability, so using Ni-rich cathode materials is only feasible if these compounds are carefully controlled to avoid oxygen release. Several research have been accomplished for solving this problem [18,23-28] such as cationic doping and coating [29-31], core–shell configuration [32], electrolyte additives [33], parasitic reactions [16], cation mixing [34], oxygen release controlling from rock-salt structure [34-40], active material removing [41], evolution of surface chemistries [29,42], which all above mentioned items are responsible for cathode degradation with Ni-richening during higher operating voltages. Basically, the first reason for the thermal runaway phenomenon is chemical interactions between the cathode and both the anode and the liquid electrolyte [43,44] during oxygen release and migration from the cathode to the anode chamber. Therefore, it is essential to prevent the surface of Ni-rich cathode materials from electrolytes. Through a triangle diagram (Figure 1), 28 composite points based on the lever rule can be determined for NMC (M= Mn, Ti, Fe, etc.), including various mole fractions of Ni, Ti, Mn, and Co (Table 1) for further synthesis. In this work, we aim to develop a novel resistive H2 sensor using the latest mechanism that enables operation in Ni-rich lithium-ion batteries, addressing several aspects, including room-temperature operation, selectivity, and internal gas sensors in LIB.

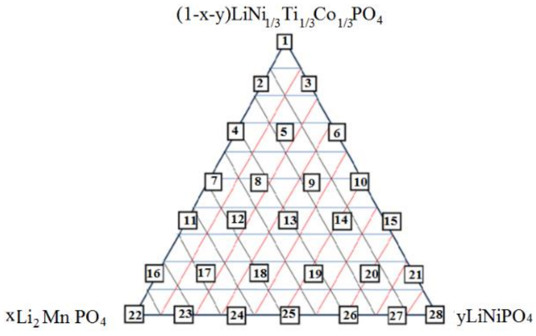

Figure 1. Binary and ternary diagram of (1–x–y) $LiNi_{0.333}Ti_{0.333}Co_{0.333}PO_4$, xLi_2MnPO4, yLiNiPO4 compositions for Ni-rich lithium-ion batteries.

As shown in Table 1, stoichiometric weights and mole fractions can be easily determined from the triangle diagram.

Table 1. 28 different composition points according to using the lever rule, stoichiometric weights, and mole fractions of the triangle diagram.

Sample	Composition	Sample	Composition
1	$LiNi_{0.333}Ti_{0.333}Co_{0.333}PO_4$	15	$LiNi_{0.778}Ti_{0.111}Co_{0.111}PO_4$
2	$Li_{1.167}Ni_{0.278}Ti_{0.278}Co_{0.278}Mn_{0.166}PO_4$	16	$Li_{1.835}Ni_{0.055}Ti_{0.055}Co_{0.055}Mn_{0.835}PO_4$
3	$LiNi_{0.444}Ti_{0.278}Co_{0.278}PO_4$	17	$Li_{1.668}Ni_{0.222}Ti_{0.055}Co_{0.055}Mn_{0.668}PO_4$
4	$Li_{1.334}Ni_{0.222}Ti_{0.222}Co_{0.222}\ Mn_{0.334}PO_4$	18	$Li_{1.501}NI_{0.389}Ti_{0.055}Co_{0.055}Mn_{0.501}PO_4$
5	$Li_{1.167}Ni_{0.389}Ti_{0.222}Co_{0.222}Mn_{0.167}PO_4$	19	$Li_{1.334}Ni_{0.556}Ti_{0.055}Co_{0.055}Mn_{0.334}PO_4$
6	$LiNi_{0.556}Ti_{0.222}Co_{0.222}PO_4$	20	$Li_{1.167}Ni_{0.723}Ti_{0.055}Co_{0.055}Mn_{0.167}PO_4$
7	$Li_{1.501}Ni_{0.167}Ti_{0.167}Co_{0.166}\ Mn_{0.500}PO_4$	21	$LiNi_{0.890}Ti_{0.055}Co_{0.055}PO_4$
8	$LiNi_{0.334}Ti_{0.166}Co_{0.166}Mn_{0.334}PO_4$	22	Li_2MnPO_4
9	$LiNi_{0.501}Ti_{0.166}Co_{0.166}Mn_{0.167}PO_4$	23	$Li_{1.835}Ni_{0.166}Mn_{0.834}PO_4$
10	$LiNi_{0.667}Ti_{0.167}Co_{0.166}PO_4$	24	$Li_{1.668}Ni_{0.332}Mn_{0.668}PO_4$
11	$Li_{1.668}Ni_{0.111}Ti_{0.111}Co_{0.111}\ Mn_{0.667}PO_4$	25	$Li_{1.501}Ni_{0.500}Mn_{0.500}PO_4$
12	$Li_{1.501}Ni_{0.278}Ti_{0.111}Co_{0.111}Mn_{0.500}PO_4$	26	$Li_{1.334}Ni_{0.668}Mn_{0.332}PO_4$
13	$Li_{1.334}Ni_{0.445}Ti_{0.111}Co_{0.111}Mn_{0.333}PO_4$	27	$Li_{1.167}Ni_{0.834}Mn_{0.166}PO_4$
14	$Li_{1.167}Ni_{0.612}Ti_{0.111}Co_{0.111}Mn_{0.166}PO_4$	28	$LiNiPO_4$

Thermal runaway arose due to Li dendrites interacting with graphite anodes during fast and long cycling, which produce flammable gases, consequently fire and explosion [45,46]. According to Global Technical Regulations for Safety of Electric Vehicles, Safety Requirements, at least five minutes before serious incidents, the early safety warning should be turned on. A safety warning sensor is based on energy storage in LIBs and acts according to the protection of the battery management system (BMS), smoke detection, and some special gases detection [47,48]. BMS sensor protects the battery through detecting its external surface increased temperature, changeable voltages, and abnormal charge density against special gases, which they produce through the Red/Ox of electrolyte materials. [49–53]. During gas accumulation inside the electrode cavity, the chamber vent ruptures and the hydrogen gas leaks sooner among other released gases (CO, CO_2, HCl, HF, and SO_2) around ten minutes earlier, before rapid temperature increasing [46, 53]. Jin and coworkers [46] exhibited that H_2 gases could be a safety index before "thermal runaway" due to the H_2 produced from the reaction of Li dendrite with polymer binders such as polyvinylidene fluoride (PVDF). However, H_2 recognizing methods in the electrode chambers of LIBs are still in an early stage of research, and there are not enough experimental data about these types of sensors. Jin et al. [54] reported on the H_2 gas diffusion mechanism and related detector installation of LIBs energy-storage chambers, which is able to turn on the warning sign around two minutes before thermal runaway in 20 ppm of H_2 concentration. Up to now, several H_2 gas sensors have been fabricated, such as FET [55–57], Schottky barrier [58–61], Capacitive [62], surface acoustic wave [63–65], and resistive [66–68]. Resistive H_2 sensors act via converting chemical reactions to the resistance signals, which has an advantage as a low detection limit (LOD) around part/per billion (ppb) mole fraction that are capable of detecting even at room temperature [69]. Palladium (Pd)-based H_2 is one of the most advanced resistive H_2 sensors, which consists of two electrodes containing one Pd-based metal and Pd-based composites [67,70–73]. Moreover, homogeneous and heterogeneous systems of other metal oxides (MOXs), carbon nanotubes (CNTs), and graphene are fabricated for detecting H_2 gas [38]. Although recent advances in information and research on resistive H2 sensors have been significant, a comprehensive integrated H2 sensor system has not yet been fabricated. According to Jin and coworkers' studies [46, 54], since the internal H_2 sensor requires more accurate sensing, it must work in the absence of any heater instrument, so the detection concentration of the internal H_2 sensor should be higher than 20 ppm. Thus, various challenges appear for this type of detection for the early safety warning of LIBs. Based on our previous work [74-82], we present a novel resistive H2 sensor mechanism that enables operation in Ni-rich lithium-ion batteries, addressing three aspects: operating at room temperature, selectivity, and internal gas sensors in LIBs.

1.1. H_2 gas sensing.

1.1.1. Li dendrite growth in LIBs.

Flammable electrolytes in LIBs and the intrinsic thermal compounds during charge and discharge can cause a problem known as battery thermal runaway. These LIB safety accidents frequently occur due to Li dendrite growth on graphite anodes under overcharging or fast charging situations [45] that depend on several factors such as type of cathode materials, type of electrolytes, and Nano anode-based materials. Here, we investigated this event on three structures of LIBs, including NMC, NCA, and NCMA. Since LIBs consist of a polymer separator and a liquid electrolyte, they are packaged in an aluminum, stainless-steel, or plastic cover [83]. We also accomplished our plan work based on a detailed schematic of a fabricated sensor for detecting mechanisms of H_2 gas through the resistive RT H_2 sensors for early safety warning of LIBs (Figure 2). This design finally achieves thermal dissipation, even at low levels, due to the battery intrinsically producing joule heat during charging or discharging, particularly under critical conditions such as overcharging or fast-cycle charging, when Li dendrites grow over the graphite anode and puncture the polymer separator [84, 85].

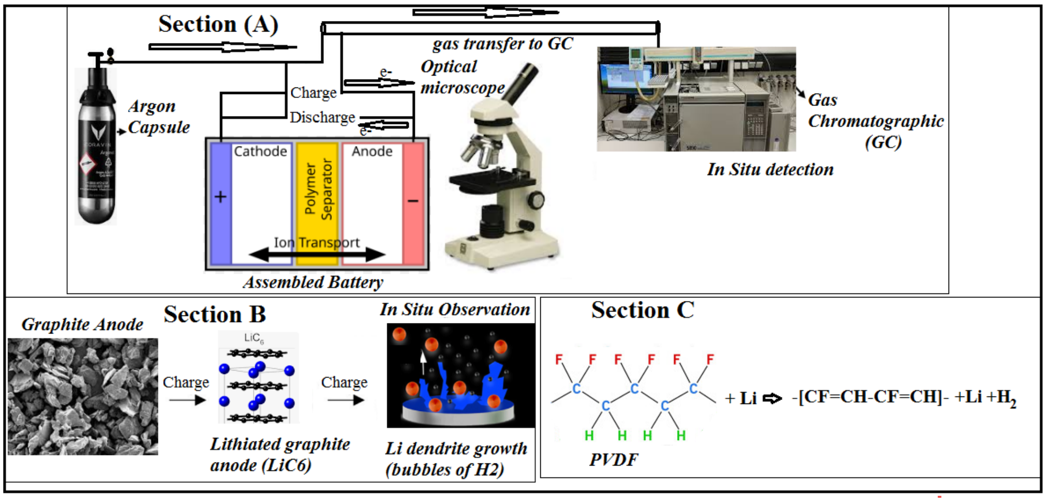

Figure 2. A simple schematic of a dendrite growth sensor through H_2 adsorption, **(A)** Optical detection of Li dendrite growth; **(B)** Mechanism of H_2 gas production; **(C)** Chemical reaction of Li and PVDF.

Consequently, a current of heat moves to the anode chamber and causes a dendrite-shorted connection, which increases violent exothermic chemical reactions and produces various gases. Safety warning sensors of battery energy storage system (BESS) basically recognize gas and smoke detection through the battery management system (BMS). These gases are produced from Red/Oxe of the electrolyte materials and cannot serve the Li dendrite growth when the temperature is less than 50°C; consequently, thermal runaway cannot be produced [86, 87]. The current BMS can recognize the external surface temperature of LIBs and the state of charge (SOC), thereby preventing a cell battery from overcharging by sending a warning signal when the external temperature exceeds [87]. Since there are large differences between the temperatures of the internal compared with the external surface of a LIB [88, 89], the error rate of SOC increases in large battery capacities (around MW-level of battery energy storage system), which is due to the poor thermal conduction of various cell components [90, 91]. Therefore, to date, SOC estimations have not been able to detect Li dendrite growth or protect the battery from safety failures, as evidenced by Tesla electric car battery fires and damage to Samsung devices. Consequently, accurate and reliable methods are needed to recognize early Li dendrite growth as a warning, allowing sufficient time for precautions.

2.2. Thermal runaway in NMC, NCA, and NCMA.

Since Li^+ ions accumulate on the surface of Ni-rich particles, including NMC, NCA, and NCMA particles, which causes destruction of electrolytes, this enhances the dissolution of metal ions (Ni, Co, Mn, and Al) in the electrolyte [92], and it decreases the Li^+ diffusion coefficient [93]. Diffusion of metal ions within the anode chamber prevents lithium migration into the anode, leading to decreased capacity and degraded battery performance [94]. Obviously, there are differences among NMC, NCA, and NCMA cathode materials about the dissolution of metal ions, where the disproportionation of Mn ions ($Mn^{3+} \rightarrow Mn^{4+} + Mn^{2+}$) can lead to more dissolution of Mn compared with Ni, Co, and Al ions [95]. Therefore, the capacity loss of LIBs is approximately dependent on the concentration of Mn ions, and obviously, the Ni-rich pristine NCA cathode exhibits much less dissolution of Ni ions than Ni-rich from NCMA, due to the stabilized effect of Al^{3+} [96]. Exceed charged situation produces large amounts of Ni^{4+}, which enables it to react with electrolytes; as a result, the thickness of the cathode-electrolyte interface (CEI) increases. This phenomenon causes a decrease in the number of Li^+, and consequently, a resistive surface layer appears [18], which in parallel increases the risk of thermal runaway in LIBs [97]. Above 4.1 V, the generation of heat due to the flow of CO2 in NMC cathode materials indicates that the metal ions react with the electrolyte, which, at the delithiated state, can cause large electrolyte oxidation. In this situation, additives should be added to the electrolyte. A mixture with 2 wt.% prop-1-ene-1,3-sultone (PES) + 2 wt.% tris-(trimethyl-silyl) phosphite (TTSPi) + 2 wt.% 1,3,2- dioxathiolane-2,2-dioxide (DTD) in the control electrolyte (1 M LiPF6 ethylene carbonate (EC): ethyl methyl carbonate (EMC) 3:7 w:w electrolyte), named PES211, should be added in electrolytes for Ni-rich cells to prevent and control the gas evolution [98]. It is notable that Ni-rich batteries should not be fully charged due to a loss of energy density [99], and additives should be added to the electrolyte to form an interphase between the cathode and the electrolyte to prevent any connection. In a Ni-rich cathode material of NMC containing graphite in an anode, the dissolved Ni moves to the anode chamber, and the tight binding between Ni^{2+} and Li^+ in the solid-electrolyte interphase (SEI) is the main reason for enhanced resistance [100]. Huang et al. applied tetravinylsilane (TVSi) as an electrolyte additive into a commercial electrolyte for $LiNi_{0.92}Mn_{0.05}Co_{0.03}O_2$ cathode [101]. As a result, the capacity exhibits retention of 83% after 200 cycles at 1°C. In another work, Zhang et al. used 3-Fluoro-5-(4,4,5,5-tetramethyl-1,3,2-dioxaborolan-2-yl)picolinonitrile (FTDP) as an additive [102]. As a result, the 1.6 Ah NMC (811)/SiO_x pouch cell with 0.2 wt.% of this additive delivered a high-capacity retention of 84.0% after 300 cycles at a current of 1.0 A.

2. Materials and Methods

2.1. Synthesis of Ni-rich cathode materials.

Since the sol-gel method makes it possible to obtain various composites, especially in the form of submicron powders, all samples were prepared using the sol-gel synthesis method, including stoichiometric weights of each compound of xLi_2MnPO_4, y $LiNiPO_4$, and (1-x-y) $LiNi_{1/3}Ti_{1/3}Co_{1/3}PO_4$ based on Figure 1 and Table 1 information. Sol-gel and molten-salt techniques were primarily used because the chemical reactions are fast and straightforward in these ternary systems compared with conventional solid-state synthesis. Particularly, it can be done at a low temperature and also has a high homogeneity in its morphologies. In the whole ternary diagram (Table 1 and Figure 1).

For finding the Ni-rich cathode materials compositions from three compounds, including (1-x-y) $LiNi_{1/3}Ti_{1/3}Co_{1/3}PO_4$, xLi_2MnPO_4, and $yLiNiPO_4$ in Figure 1 mixtures, stoichiometric weights and suitable mole-fractions were chosen to synthesize those optimized materials with good electrochemical efficiency and high initial discharge capacities. According to different composition points, using the lever rule, 8 samples from 28 added were selected with numbers 1, 6, 13, 15, 19, and 25, which are Ni-rich compared with other compositions. The condition of synthesis and details of materials usage and the names of companies, as well as related electronic devices, were exactly described in our previous work, completely [103]. Titanium and Cobalt mole fractions gradually reduced towards the down direction of the triangle; meanwhile, the compositions of 22 and 24 have zero mole fractions of Titanium and Cobalt. More amounts of manganese are found in sample 22, and its amount decreases at the opposite endpoints of the triangle. The notable cyclability of the samples is directly related to the amounts of Manganese, Cobalt, Titanium, and Nickel, as well as the specific capacities of all samples, which are related to the energy that can be stored per unit volume or mass (Ah).

2.2. Characterization of 6 composites.

2.2.1. XRD and morphological features of the samples.

X-ray diffraction of (1–x–y) $LiNi_{0.333}Ti_{0.333}Co_{0.333}PO_4$, xLi_2MnPO_4, $yLiNiPO_4$ is shown in Figure 3. XRD was done for six composites, using inductively coupled plasma atomic emission spectroscopy (ICP-AES) devices (ICP analyzers; PerkinElmer Optima 7300 DV containing ASX-520 auto sampler). XPS (Cu-Kα radiation with $\lambda = 1.49$ Å) was used to define the percentage amount and the oxidation number of the transition metals, including Ti, Ni, Mn, and Co, to confirm the exact morphology of those samples. The θ angles for each sample with sharp peaks were seen according to Bragg’s law to distinguish the existence of any unknown substances via diffraction data (Table 2).

Table 2. lattice constants and peak intensities of six composites.

Sample	a (nm)	c (nm)
1	0.263	1.4
25	0.271	1.5
6	0.274	1.5
13	0.285	1.3
15	0.280	1.5
19	0.275	1.4

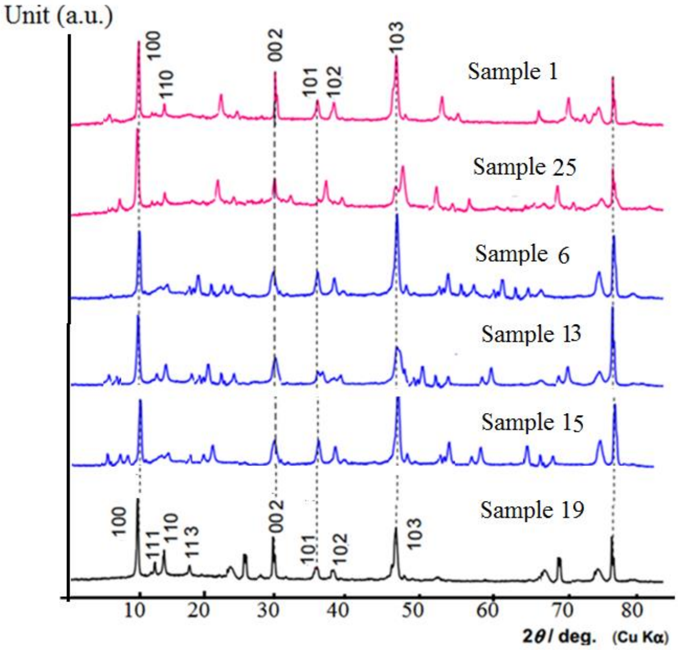

Figure 3. X-ray diffraction of six cathodic composites combination of (1–x–y) $LiNi_{0.333}Ti_{0.333}Co_{0.333}PO_4$, xLi_2MnPO_4, $yLiNiPO_4$.

2.2.2. Raman analysis.

Raman peaks were used to predict the structure and cathode material properties of all samples. Figure 4 exhibits spectra of the pure $LiNi_{0.333}Ti_{0.333}Co_{0.333}PO_4$, Li_2MnPO_4, and $LiNiPO_4$, including samples 1, 13, and 15 from Table 1. The highest peak at 700 cm^{-1} (A1g) belongs to the $LiNi_{0.333}Ti_{0.333}Co_{0.333}PO_4$ in structures with the group theory model of (P21/n). Although the peaks of $LiNiO_2$ and $LiCoO_2$ are 425 cm^{-1} (Eg) and 225 cm^{-1} (T2g) respectively, but these amounts will changed a little bit in mixture samples of(1–x–y) $LiNi_{0.333}Ti_{0.333}Co_{0.333}PO_4$, xLi_2MnPO_4, $yLiNiPO_4$. The peak widths indicate stability due to the uncertainty principle of the Heisenberg rule.

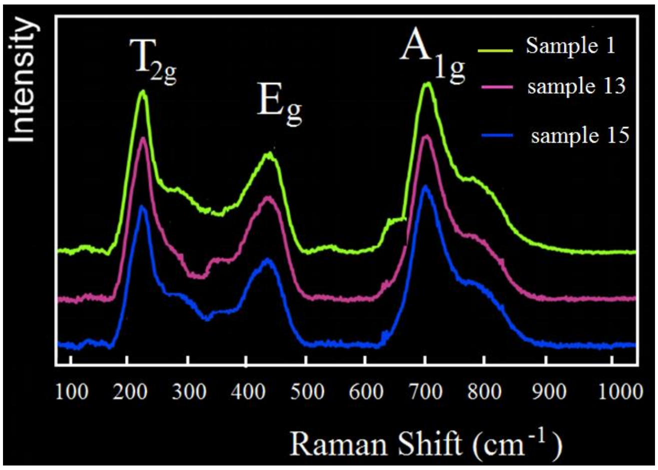

Figure 4. Raman spectra shift (cm^{-1}); contains samples 1, 13, 15 from table 1.

The width of the energies and also the time-dependent can be described by the Heisenberg rule because the Heisenberg uncertainty principle can be interpreted as: $\Delta E.\Delta t \geq \hbar/2$, where h is Planck's constant (~4×10^{-15} eVs) and Δt @$t_{1/2}$ (~10^{-16} s) is the half-life of the initial ionization position. So, $\Delta E \geqslant \hbar/2\Delta t$ ~6 eV indicates the natural Auger line width (G). During $\Delta E_{instrument} \geqslant$G, instrumental broadening occurs, but if ΔE instrument is significantly less than G, the effect on peak width by the instrument is small. Since the photon energy and the wavelength are related as $= \frac{2\pi\hbar c}{\lambda}$, the uncertainty relation of the width peak can be found by $\Delta\varepsilon = \frac{2\pi\hbar c}{\lambda^2}\Delta\lambda$. Consequently, the position and the place of Raman peaks are a factor for recognition of each sample.

In Figure 4, the internal modes are assigned as $v1$, $v2$, and $v3$ as T_{2g}, E_g, and A_{1g}, respectively. It is notable in this work that the laser light of the Raman spectroscopy was selected to be smaller than 1 µm.

2.2.3. SEM, TEM and HRTEM.

The morphology of the powder samples was analyzed using SEM (SU3900, Hitachi, Ltd., Tokyo, Japan) and the HT7800 Ruli TEM (HT7800, Hitachi, Ltd., Tokyo, Japan) (Figure 5).

The surface structures of active materials for 10 samples were examined using spherical-aberration-corrected (Cs)-STEM (JEOL, JEM-ARM200F, 200kV) and HRTEM (JEOL, JEM-3010), with energy-dispersive X-ray spectroscopy (EDX) and electron energy-loss spectroscopy. TEM images showed that the lithium-transition metal in the mixed layered oxides exhibits excellent homogeneity in metal distribution, and the presence of metal cation mixing in each sample has been confirmed at a proper mole ratio. Using HRTEM, we characterized the TNMC particles in each sample and their concentration at the macroscopic scale.

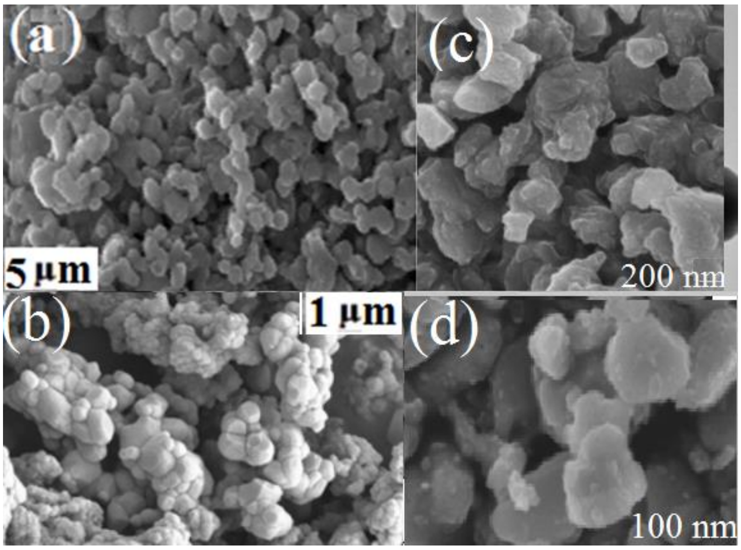

Figure 5. SEM **(a,b)**; TEM **(c,d)** images of sample 15 on micro and nano scales.

2.3. Li-dendrite growth sensor during H_2 gas adsorption.

An in situ optical system for sensing H_2 gas amounts was designed based on Figure 2 to exhibit Li dendrite growth via H_2 gas adsorption with various cathode materials of the above-mentioned samples, produced gases (Figure 2A) from a self-assembled LIB, including various Ni-rich cathode materials, graphite-based anode materials, and a liquid electrolyte of $LiPF_6$ dissolved in organic solvent of EC (ethylene carbonate). In addition to evaluating the conductive pathway for the movement of cations passing from the negative to the positive electrodes during discharge, we also used $LiBF_4$, $LiClO_4$, dissolved in EMC (ethyl methyl carbonate) and PC (propylene carbonate), respectively, and frequently. These materials were located in a glass package and were attached to a GC instrument for automatic detection at any time under Ar gas. In addition, PVDF (Polyvinylidene Fluoride) was used in our system due to its high thermal level and electrochemical stability. It is notable that the degradation of PVDF binder also causes the destruction of electroactive materials and the loss of cycling charge. Dendrite formation can be recorded simultaneously via optical microscopy, and in a usual position, Li ions are deintercalated from the cathode and intercalated into the graphite anode, leading to LiC_6 formation [104]. We measured the dendrite production by optical microscopy gradually. Based on the destruction and decomposition mechanism, the Li ions are first separated from the cathode and intercalated into the graphite anode to form LiC_6. Under overcharging or fast cycling charging, Li dendrites start growing on Li-saturated parts of the graphite anode and react with polymer binder (PVDF), thus generating H_2 gas (Figure 2 B) [105]. Figure 2-c and Figure 6 exhibited the mechanism of Li-PVDF interactions that gradually produce hydrogen bubbles.

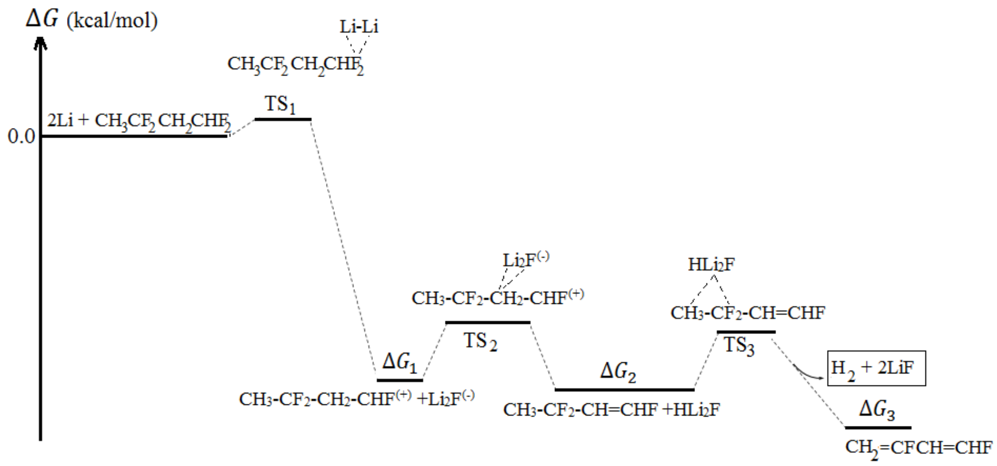

Figure 6. Gibbs energies changing for the degradation mechanism of lithium metal over PVDF binder reaction

Since H_2 gas comes out from the lithium and PVDF reaction according to the stoichiometric amount as follows $-CH_2-CF_2-+Li \rightarrow LiF + -CH=CF- +0.5\,H_2$

The corresponding size of Li dendrite formation based on released H_2 gas concentration, we have to suppose the minimal H_2 amount as 4.5×10^{-5} mg at 20°C under 1 atmosphere pressure. This is equivalent to a Li-metal particle with a radius of approximately 50 μm or equal 2.8×10^{-4} mg plated on the graphite anode, which can result in detectable H_2 generation by gas chromatography.

3. Results and Discussion

3.1. In situ detection of H_2 gas.

In situ experiments were conducted as shown in Figure 2, using a platform containing synthesized composites intercalated into graphite. Composites of graphite and Li metal-graphite were used as cathodic and anodic electrodes, respectively. Meanwhile, both graphite electrodes contained vacuum-dried PVDF and carbon black with a mass ratio of 6:1:1; for graphite// carbon black// PVDF, respectively. Two electrodes were fixed at a distance of 5 mm from each other (Figures 7a and b), and the overlap area of the two electrodes was designed to be 4 cm^2. The theoretical area capacity of graphite anode was 1mAhcm^{-2}, and the charging current density was set as 4 mAhcm^{-2} (1 mA/ cm^2) (equivalent to 1°C rate).

In situ measuring of cathodic composites based on graphite cells exhibited growing H_2 gas from composite samples dendrites, as well as a similar event, H_2 gas is also generated from the Li dendrites due to the metal that can be reacted with the polymer binder in the graphite electrode.

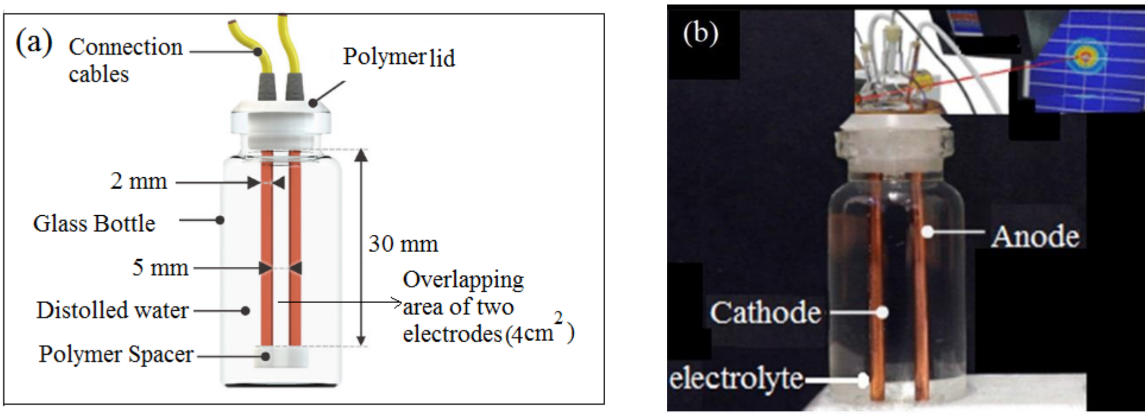

Figure 7. Detailed structure of situ lithium batteries: **(a)** schematic image of anodic and cathodic structure and dimension; **(b)** Fabricated bottle containing two electrodes and electrolyte containing related cables and monitor.

To remove the heat effect from internal resistance during Li metal-PVDF connections and charging, thermal simulations of self-assembled cells were performed using the finite element method. The whole charging time was about 2000 seconds (Figure 8a and b), and during this time, the simulated temperature slightly increased (around 0.25°C). Therefore, according to the room temperature at 20°C, the maximum temperature was about 20.25°C throughout the whole of the measurement. Obviously, this negligible temperature change is low enough to cause localized heating that affects the reaction, and during this time, the simulated temperature change with a slightly increased rate of the cell has been plotted for six composite samples (Figure 8c).

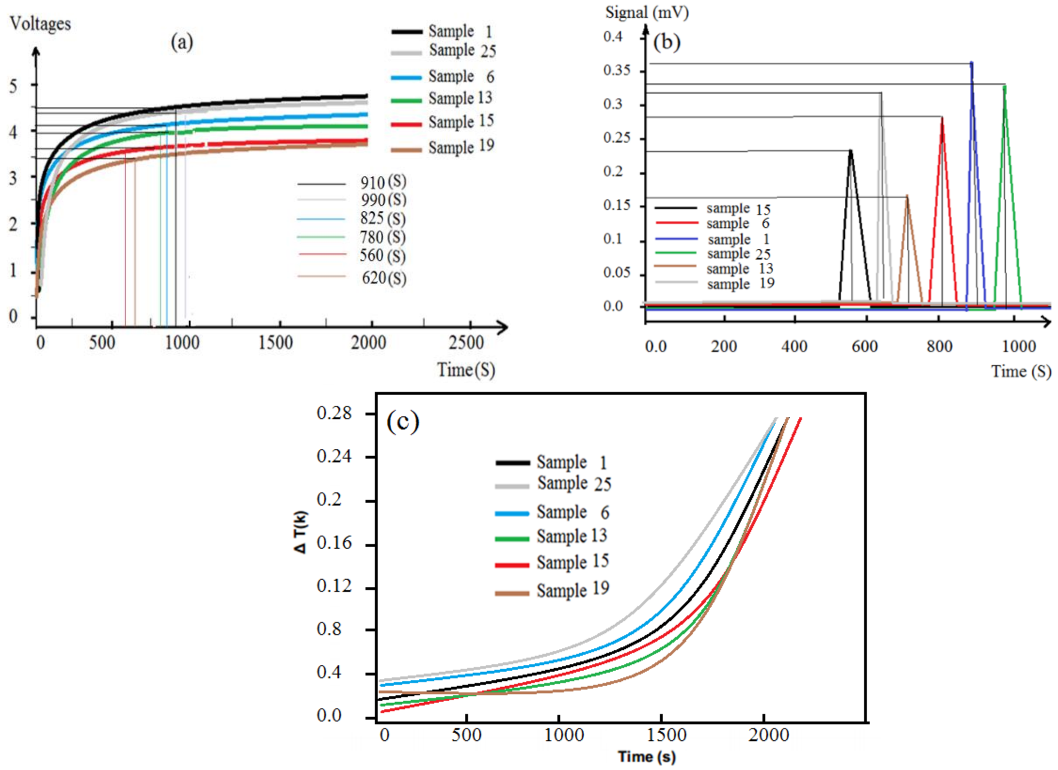

Figure 8. Anode area (4cm^2) charge current (4 mAh cm^{-2}); **(a)** Voltage Vs time of self-assembled for samples 1,6,13,15,19,25 of composite-graphite in LIBs; **(b)** The signals voltages (mV) of six samples from 1, 25, 6, 13, 15; **(c)** Slightly increased rate of the cell for six composite samples. For the samples-graphite cell, SOC begins from 0% at 0 s, and Li dendrite growth has been detected at 910, 990,825,780, 560, and 620 seconds for samples including 1, 25,6,13,15, and 19, respectively. The cell voltages were also around 4.4, 4.5, 4.1, 3.95, 3.65, and 3.48 approximately and respectively (Figure 8-a).

Since calibration is an important process, the measurements obtained from the GC were calibrated by known standards to establish a reliable basis for accurate analysis. Calibration ensures that the GC system can accurately translate sample concentrations into meaningful data points, which is essential for making informed decisions based on the analysis. By ensuring the GC system is properly calibrated, we are able to trust the data it generates. Gradually, H_2 gas starts to be produced due to the Li dendrite phenomenon, and consequently, a signal can be detected through gas chromatography, and H_2 bubbles can also be observed through optical microscopy simultaneously. Due to the resolution limitation of microscopy, the initial dendrite can be smaller than 1 mm and forms much earlier than 560 s (Figure 8b). The signal voltages (mV) of these six samples from 1, 25, 6, 13, 15, and 19 are 0.37, 0.34, 0.28, 0.16, 0.24, and 0.32 millivolts, respectively. The time of appearance of these signals in Figure 8-b for each composite is also approximately similar to the time of appearance in Figure 5a corresponding to the composites. Although in this work, we are looking to find a novel sensor using the latest mechanism for resistive H_2 sensors that enable working in Ni-rich lithium-ion batteries based on three aspects, including operating at room temperature, selectivity, and internal gas sensors in LIB, there are several limitations for Ni-rich lithium-ion batteries as follows. 1- The high redox potential of Ni-rich cathode materials is the cause for their poor thermal and structural stability [21, 22]; 2-using Ni-rich cathode materials is runnable only if this compounds is controlled for avoiding oxygen releasing [23]; 3-During oxygen releasing and migrate from cathode to anode preventing the surface of Ni-rich cathode materials from electrolytes is very important compared with other commercial LIBs. 4- Exceed Li^+ ion accumulation on the surface of Ni-rich, including NMC, NCA, and NCMA particles, causes the destruction of electrolytes quickly. 5-The Ni-rich batteries should not be fully charged due to loss of energy density [99]; 6- When using Ni-rich batteries, additives should be added to the electrolyte to produce an interphase between cathode-electrolyte for preventing any connection [99]. According to these items, an index item containing the H_2 gas signal detecting time multiplication to voltage signals in Figure 8b can be used to show the efficiency of each sample for applying in electric vehicle (EVs) systems. These amounts are 333.6. 336.6, 231.56, 218.4, 134.4, and 198.4 for samples 1, 25, 6, 13, 15, and 19, respectively. Therefore, sample 15 $LiNi_{0.778}Ti_{0.111}Co_{0.111}PO_4$, with the most Ni-rich, exhibited better efficiency compared with other samples.

2.2. Battery modelling and sensor faults.

2.2.1. Resistance circuit for predication of an accurate ECM parameter.

In this work, we designed and fabricated a planar model based on fault detection and isolation (FDI) for Ni-rich LIBs undergoing degradation [106, 107]. Currently, battery degradation can be prevented by fitting experimental data in situ testing of EV conditions. We should be able to estimate the equivalent circuit model (ECM) parameters in real-time and in situ testing. Obviously, in advanced EVs, we need a battery management system (BMS) [108] with high efficiency and accuracy to ensure safety. The major functions of the BMS should cover two important items, including SOC and state of health (SOH) over both current and voltage protection. Since ECM parameters can be generated during degradation, the FDI scheme estimates ECM parameters in real time using a weighted moving average (WMA) to detect faults in voltage and current sensors. Fault detection and isolation (FDI) of EVs plans can be improved via integrating degradation into the Schematic of a resistance equivalent circuit model (ECM) as follows (Figure 9). In an FDI approach using fundamental analysis and statistical theory, ECM estimation can be checked; therefore, an FDI scheme using output error with findings that exhibited false can be operated by model parameters [109].

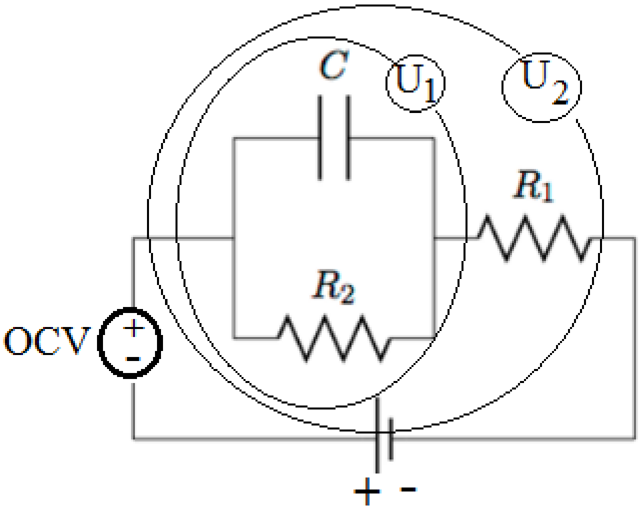

Figure 9. Schematic of a resistance equivalent circuit model (ECM).

The resistance monitoring in any EVs for our sensor can be expressed as follows:

$$U_1 = \frac{1}{C} - \frac{U_1}{CR_2} \text{ and } U_{eq} = OCV - U_1 - IR_2 \qquad (1)$$

Here, the system enables obtaining the transfer function of the battery impedance from Equation (1), according to Equation (2), then the transfer function can be discretized using the Euler transformation:

$$G(s) = \frac{U_2(s)}{I(s)} = -R_1 - \frac{R_2}{1+sR_2C} \; and \; G(z) = \frac{a_{2+a_3Z^{-1}}}{1+a_1Z^{-1}} \qquad (2)$$

$$\text{where } a_1 = \frac{T}{R_2C} - 1, a_2 = -R_1, \text{ and } a_3 = R_1 - \frac{T}{C} - \frac{TR_1}{R_2C} \quad (3)$$

Consequently, the amounts of OCV (open-circuit voltage) will be determined from the above resistance equations (equations 1-3), which can also be established for predicting accurate ECM parameter estimations for the purpose of fault diagnosis. This work focuses on sensor faults, and measurements from voltage and current sensors can affect the estimation of SOC. It is notable that a voltage-accuracy system used to calculate SOC in a Lithium iron phosphate (LFP) cell has a base error of 5.9%, whereas a lithium nickel manganese cobalt oxide (NMC) cell's SOC can have different base errors [110].

4.2.2. Experimental setup.

Here we used a simple testing setup assembled by a battery tester, Maccor 4200, and this system was connected to a computer that had a software program for controlling the battery test system to charge and discharge the cell at a room temperature of 25°C, as well as it was run from the cell SOC of 15% to 85% (Figure 10).

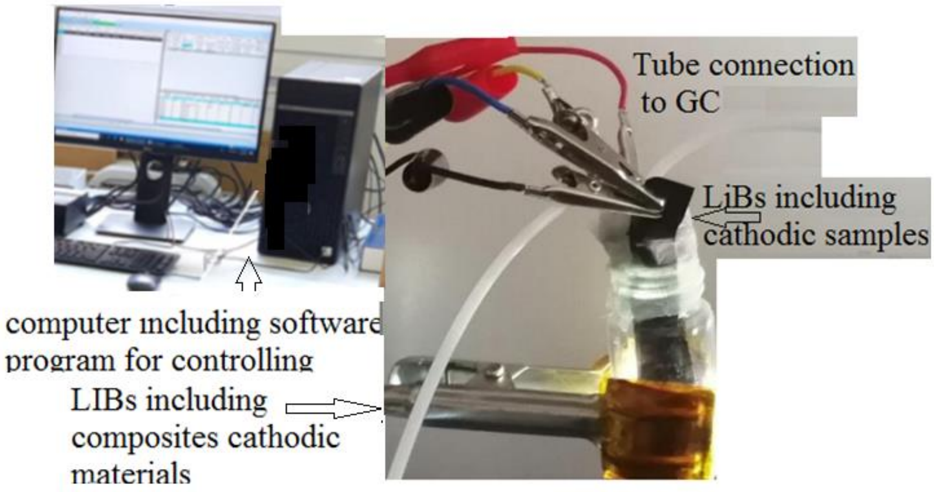

Figure 10. Experimental setup for ECM estimation of various samples composites (Ni-reached samples of 1, 6, 13, 15, 19, and 25) in real-time and in situ testing.

Figure 11 exhibits the degradation effects of R_1, R_2, and C parameters for six cathodic material composites. As can be seen in all items, the effect of degradation on R_1 does not exhibit any obvious change. However, it can be distinctly seen that R_2 increases, while C decreases, with degradation. This is a reasonable trend because the R_2-C pair (Figure 9) represents the charge-transfer, and degradation can affect the total charge in the cell battery. Although any changes of these parameters are not considerable in a short time by a few drive cycles, they can be very considerable in the whole lifetime for any lithium battery cells, particularly in rich nickel cathodic materials.

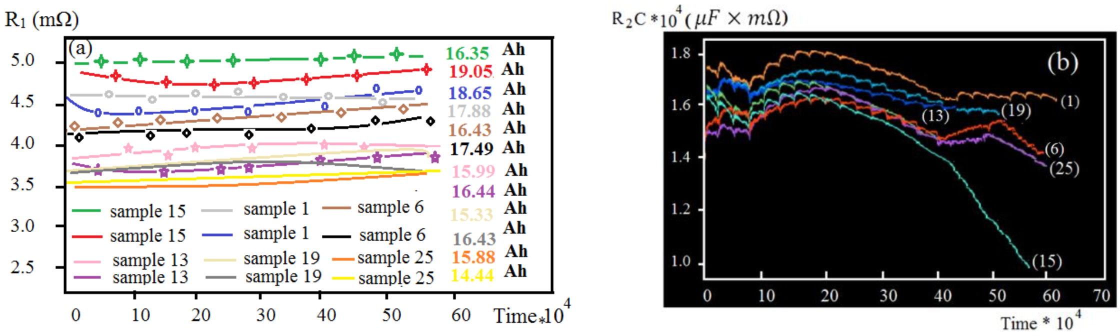

Figure 11. ECM parameters evaluation at various cell capacities. (**a**) R_1 estimation at different cathodic samples cell capacities; (**b**) R_2C estimation at different cathodic samples cell capacities.

Interestingly, by several simulations, it was shown that R1 responds the fastest to current sensor faults, while either R2 or C2 responds the fastest to voltage sensor faults. According to these facts, we are able to investigate a fault isolation plan to complement the detection method.

4.3.3. Voltage sensor fault detection.

In this work, multiple voltage sensors for 6 samples were tested, as faults were estimated at different cell capacities. The voltage sensor faults at different cell capacities were exhibited in Table 3. We found sample 15 as the sensitive Ni-rich composite for cathode materials in LIBs (Figure 12).

Table 3. Voltage sensor faults at different cell capacities.

Samples	**Composition**	**Capacity (Ah) Range**	**Fault Voltage *Detection***	**Detection time (R_2C)**
1	$LiNi_{0.333}Ti_{0.333}Co_{0.333}PO_4$	17.55-18.40	0.45-0.50	34000

Samples	Composition	Capacity (Ah) Range	Fault Voltage *Detection*	Detection time (R_2C)
6	$LiNi_{0.556}Ti_{0.222}Co_{0.222}PO_4$	16.34-17.30	0.50-0.55	33000
13	$Li_{1.334}Ni_{0.445}Ti_{0.111}Co_{0.111}Mn_{0.333}PO_4$	15.88-16.25	0.55-0.58	34000
15	$LiNi_{0.778}Ti_{0.111}Co_{0.111}PO_4$	16.12-18.95	0.51-0.59	31000
19	$Li_{1.334}Ni_{0.556}Ti_{0.055}Co_{0.055}Mn_{0.334}PO_4$	15.12-16.55	0.49-0.52	32000
25	$Li_{1.501}Ni_{0.500}Mn_{0.500}PO_4$	14.22-16.40	0.48-0.56	33000

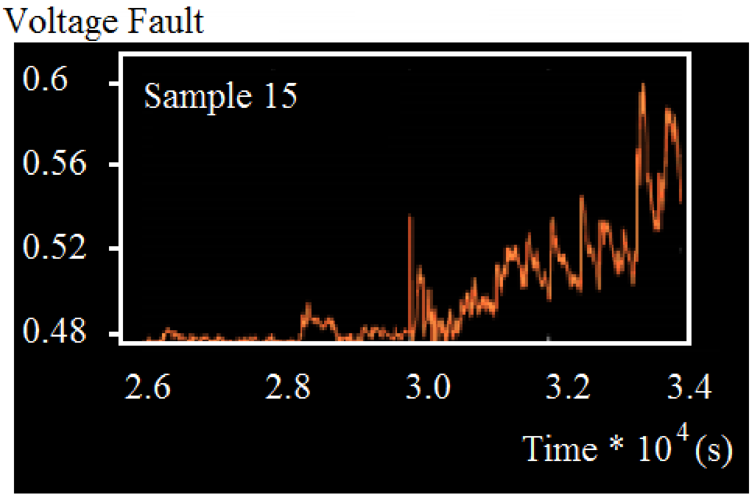

Figure 12. Detecting result in the case of voltage sensor fault versus time for sample 15.

4.3.4. Current sensor fault detection.

Similar to voltage sensor fault diagnosis validation, current sensor faults were also found for various composite samples. The diagnostic results are plotted in Figure 13 according to data from Table 4. This paper also presented a model-based sensor FDI scheme for a Li-ion cell used in EVs with cell degradation consideration.

Table 4. Amperage sensor faults at different cell capacities.

samples	Composition	Capacity (Ah) Range	Faults Amperage Detection (A)	Detection time (R_2C)
1	$LiNi_{0.333}Ti_{0.333}Co_{0.333}PO_4$	17.55-18.40	1.45-3.40	28500
6	$LiNi_{0.556}Ti_{0.222}Co_{0.222}PO_4$	16.34-17.30	1.65-3.75	30900
13	$Li_{1.334}Ni_{0.445}Ti_{0.111}Co_{0.111}Mn_{0.333}PO_4$	15.88-16.25	1.55-3.65	31500
15	$LiNi_{0.778}Ti_{0.111}Co_{0.111}PO_4$	16.12-18.95	1.15-3.75	29500
19	$Li_{1.334}Ni_{0.556}Ti_{0.055}Co_{0.055}Mn_{0.334}PO_4$	15.12-16.55	1.35-3.40	31000
25	$Li_{1.501}Ni_{0.500}Mn_{0.500}PO_4$	14.22-16.40	1.65-3.85	32000

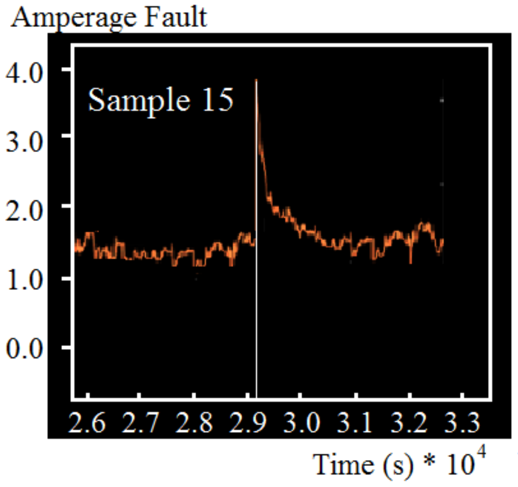

Figure 13. Detecting result in the case of amperage sensor fault versus time for sample 15.

In addition, the errors were found to increase during fault injection, indicating a current sensor fault according to the FDI plan. Consequently, assuming constant parameters in fault detection and isolation (FDI) is not sufficient for any evaluation, and the acceptable data for the FDI plan should account for parameter changes from ECM due to cell degradation.

In addition, data collected after sampling and the readings were analyzed with calibration procedures, and also statistical analysis was done, like descriptive statistics, correlation, regression, and predicting the average voltages and capacity (Ah), ranges from the regression equation were obtained with RMSE=0.99 in all items.

4. Conclusions

Thermal runaway arose due to Li dendrites interacting with graphite anodes during fast and long cycling, which produces the generation of flammable gases, consequently, fire and explosion. Based on the Global Technical Regulations for the Safety of Electric Vehicles, Safety Requirements, the early safety warning should be activated at least 5 minutes before serious incidents. Therefore, we developed a sensitive detection method for Li dendrite growth in LIBs by H_2 gas capture for early safety warning, containing six synthesized Ni-rich composites. We designed and fabricated a temperature- and resistance-monitoring sensor for detecting Li dendrite growth in LIBs using H_2 gas capture, providing early safety warnings from six synthesized Ni-rich novel composites. We found the minimum size of metallic Li dendrites that can be detected is only 2.8×10^{-4} mg.

Through gas detection tests with six synthesized cathodic materials in a battery tube pack in situ cabin, H_2 gas was found to be the most suitable gas for sensing, which enables capturing much faster than the other gases. The Li dendrite growth and thermal accumulation process can be intercepted from the cell by cutting off charging at the time H_2 gas is captured, with neither smoke nor fire observed. It is notable that the $LiNi_{0.778}Ti_{0.111}Co_{0.111}PO_4$ composite containing a faulty voltage of 0.51-0.59 and a detection time of (R2C=31000) seconds, as well as a capacity (Ah) range between 16.12-18.95 and faulty amperage detection (A) between 1.15-3.75, has the most efficiency and safety warning for electric vehicle usage compared with other samples in Ni-rich cathode materials. Finally, we found that our novel synthesized composite, $LiNi_{0.778}Ti_{0.111}Co_{0.111}PO_4$, has the highest efficiency and safety for electric vehicle use compared with other samples in Ni-rich cathode materials.

Author Contributions

Conceptualization, M.M. and M.M.; methodology, F.M.; software, M.A. and Z.S.; validation, M.M., M.A., and A.M.; formal analysis, M.M.; investigation, A.M.; resources, M.A.; data curation, Z.S. and M.A.; writing—original draft preparation, Z.S. and A.M.; writing—review and editing, M.M.; visualization, M.M.; supervision, M.M.; project administration, M.M.; funding acquisition, F.M. All authors have read and agreed to the published version of the manuscript.

Institutional Review Board Statement

Not applicable.

Informed Consent Statement

Not applicable.

Data Availability Statement

Not applicable.

Funding

This research received no funding.

Acknowledgments

The authors thank Islamic Azad University and Kastamonu University for providing facilities, as well as the authors whose names were cited in the references for their cooperation, support, and like-mindedness.

Conflicts of Interest

The authors declare no conflict of interest.

References

1. You, L.Z.; Chu, B.B.; Li, G.X.; Huang, T.; Yu. A.S. H_3BO_3 washed $LiNi_{0.8}Co_{0.1}Mn_{0.1}O_2$ with enhanced electrochemical performance and storage characteristics. *J. Power Sources* **2021**, *482*, 228940, https://doi.org/10.1016/j.jpowsour.2020.228940.
2. Yu, H.; Cao, Y.; Chen, L.; Hu, Y.; Duan, X.; Dai, S.; Li, C.; Jiang, H. Surface enrichment and diffusion enabling gradient-doping and coating of Ni-rich cathode toward Li-ion batteries. *Nat. Commun.* **2021**, *12*, 4564, https://doi.org/10.1038/s41467-021-24893-0.
3. Rajkamal, A.; Sharma, A.; Pullagura, B.K.; Thapa, R.; Kim, H. Engineering lithium nickel cobalt manganese oxides cathodes: A computational and experimental approach to bridging gaps. *Chem. Eng. J.* **2024**, *481*, 148223, https://doi.org/10.1016/j.cej.2023.148223.
4. Ding, H.; Wang, X.; Wang, J.; Zhang, H.; Liu, G.; Yu, W.; Dong, X.; Wang, J. Morphology-controllable synthesis and excellent electrochemical performance of Ni-rich layered NCM622 as cathode materials for lithium-ion batteries via glycerin-assisted solvothermal method. *J. Power Sources* **2023**, *553*, 232307, https://doi.org/10.1016/j.jpowsour.2022.232307.
5. Kim, J.; Lee, I.; Kim, Y.-H.; Bae, J.H.; Hwang, K.; Kang, H.; Shim, J.-H.; Kim, J.-S.; Park, C.W.; Kim, Y.-M. Ni-rich cathode material with isolated porous layer hindering crack propagation under 4.5 V high cut-off voltage cycling. *Chem. Eng. J.* **2023**, *455*, 140578, http://dx.doi.org/10.2139/ssrn.4263651.
6. Liu, H.; Zhu, Z.; Yan, Q.; Yu, S.; He, X.; Chen, Y.; Zhang, R.; Ma, L.; Liu, T.; Li, M. A disordered rock salt anode for fast-charging lithium-ion batteries. *Nature* **2020**, *585*, 63-67, https://doi.org/10.1038/s41586-020-2637-6.
7. Xie, H.; Peng, H.; Jiang, D.; Xiao, Z.; Liu, X.; Liang, H.; Wu, M.; Liu, D.; Li, Y.; Sun, Y.; Zhong, S.; Qian, Z.; Wang, R. Structures, issues, and optimization strategies of Ni-rich and Co-low cathode materials for lithium-ion battery. *Chem. Eng. J.* **2023**, *470*, 144051, https://doi.org/10.1016/j.cej.2023.144051
8. Tian, X. Guo, R. Bai, Y. Li, N. Wang, X. Wang, J. Wu, C. High-performance high-nickel multi-element cathode materials for lithium-ion batteries. *Batteries* **2023**, *9*, 319, https://doi.org/10.3390/batteries9060319.
9. Ryu, H.-H.; Namkoong, B.; Kim, J.H.; Belharouak, I.; Yoon, C.S.; Sun, Y.K. Capacity fading mechanisms in Ni-rich single crystal NCM cathodes. *ACS Energy Lett.* **2021**, *6*, 2726–2734, https://doi.org/10.1021/acsenergylett.1c01089.
10. Maleki, H.; K. Sari, H.M.; Li, X. Controllable cathode–electrolyte interface of Li [Ni0.8Co0.1Mn0.1]O2 for lithium ion batteries: a review. *Adv. Energy Mater.* **2019**, *9*, 1901597, https://doi.org/10.1002/aenm.201901597.

11. S. Mubarac, Silva, M.N.T.; Silva, G.T.M.; Freitas, B.; Gonçalves, J.; Zanin, H. *Super* Ni-rich and Co-poor $LiNi_xCo_yMn_{1-x-y}O_2$, $LiNi_xCo_yAl_{1-x-y}O_2$, and $LiNi_xCo_yMn_zAl_1$-$x_{-y-z}O_2$ ($x \geq 0.85$) based cathodes for lithium-ion batteries: A review on emerging trends, recent developments, and future perspectives. *J. Energy Storage* **2024**, *96*, 112612, https://doi.org/10.1016/j.est.2024.112612.
12. Li, J.; Manthiram, A. A comprehensive analysis of the interfacial and structural evolution over long-term cycling of ultra- high-nickel cathodes in lithium-ion batteries. *Adv. Energy Mater.* **2019**, *9*, 1902731, https://doi.org/10.1002/aenm.201902731.
13. Cui, Z.; Xie, Q.; Manthiram, A. Zinc-doped high-nickel, low-cobalt layered oxide cathodes for high-energy-density lithiumion batteries. *ACS Appl. Mater. Interfaces* **2021**, *13*, 15324–15332, https://doi.org/10.1021/acsami.1c01824.
14. Li, J.; Liu, H.; Xia, J.; Cameron, A.R.; Nie, M.; Botton, G.A.; Dahn, J.R. The impact of electrolyte additives and upper cut-off voltage on the formation of a rocksalt surface layer in $LiNi_{0.8}Mn_{0.1}Co_{0.1}O_2$ electrodes. *J. Electrochem. Soc.* **2017**, *164*, A655–A665, https://doi.org/10.1149/2.0651704jes.
15. Xu, C.; Märker, K.; Lee, J.; Mahadevegowda, A.; Reeves, P.J.; Day, S.J.; Groh, M.F.; Emge, S.P.; Ducati, C.; Mehdi, B.L.; Tang, C.C.; Grey, C.P. Bulk fatigue induced by surface reconstruction in layered Ni-rich cathodes for Li-ion batteries. *Nat. Mater.* **2021**, *20*, 84–92, https://doi.org/10.1038/s41563-020-0767-8.
16. Li, J.; Downie, L.E.; Ma, L.; Qiu, W.; Dahn, J.R. Study of the failure mechanisms of $LiNi_{0.8}Mn_{0.1}Co_{0.1}O_2$ Cathode material for lithium ion batteries. *J. Electrochem. Soc.* **2015**, *162*, A1401–A1408, https://doi.org/10.1149/2.1011507jes.
17. Zhang, N.; Li, J.; Li, H.; Liu, A.; Huang, Q.; Ma, L.; Li, Y.; Dahn, J.R. Structural, electrochemical, and thermal properties of nickel-rich $LiNi_xMn_yCo_zO_2$ materials. *Chem. Mater.* **2018**, *30*, 8852–8860, https://doi.org/10.1021/acs.chemmater.8b03827.
18. Schipper, F.; Erickson, E.M.; Erk, C.; Shin, J.-Y.; Chesneau, F.F.; Aurbach, D. Review: recent advances and remaining challenges for lithium-ion battery cathodes. *J. Electrochem. Soc.* **2017**, *164*, A6220–A6228, https://doi.org/10.1149/2.0351701jes.
19. Kim, M.; Zhu, J.; Li, L.; Wang, C.; Chen, G. Understanding reactivities of Ni-rich Li[NixMnyCo1-x-y]O2 single-crystal cathode materials. *ACS Appl. Energy Mater.* **2020**, *3*, 12238–12245, https://doi.org/10.1021/acsaem.0c02278.
20. Xu, J.; Lin, F.; Doeff, M.M.; Tong, W. A review of Ni-based layered oxides for rechargeable Li-ion batteries. *J. Mater. Chem. A* **2017**, *5*, 874–901, https://doi.org/10.1039/C6TA07991A.
21. Duh, Y.S.; Sun, Y.; Lin, X.; Zheng, J.; Wang, M.; Wang, Y.; Lin, X.; Jiang, X.; Zheng, Z.; Zheng, S.; Yu, G. Characterization on thermal runaway of commercial 18650 lithium-ion batteries used in electric vehicles: A review. *J. Energy Storage* **2021**, *41*, 102888, https://doi.org/10.1016/j.est.2021.102888.
22. Ohneseit, S.; Finster, P.; Floras, C.; Lubenau, N.; Uhlmann, N.; Seifert, H.J.; Zizebert, C. Thermal and mechanical safety assessment of type 21700 lithium-ion batteries with NMC, NCA and LFP cathodes–investigation of cell abuse by means of accelerating rate calorimetry (ARC). *Batteries* **2023**, *9*, 237, https://doi.org/10.3390/batteries9050237.
23. Mollaamin, F.; Monajjemi, M. Doping of Graphene Nanostructure with Iron, Nickel and Zinc as Selective Detector for the Toxic Gas Removal: A Density Functional Theory Study. *C* **2023**, *9*, 20, https://doi.org/10.3390/c9010020.
24. Manthiram, A. An outlook on lithium-ion battery technology. *ACS Cent. Sci*. **2017**, *3*, 1063–1069, https://doi.org/10.1021/acscentsci.7b00288.
25. Singh, J.P.; Devnani, H.; Sharma, A.; Lim, W.C.; Dhyani, A.; Chae, K.H.; Lee, S. Challenges and opportunities using Ni-rich layered oxide cathodes in Li-ion rechargeable batteries: the case of nickel cobalt manganese oxides. *Energy Adv*. **2024**, *3*, 1869–1893, https://doi.org/10.1039/D3YA00631J.
26. Ahangari, M.; Szalai, B.; Lujan, J.; Zhou, M.; Luo, H. Advancements and challenges in high-capacity Ni-rich cathode materials for lithium-ion batteries. *Materials* **2024**, *17*, 801, https://doi.org/10.3390/ma17040801.
27. Butt, A.; Ali, G.; Kubra, K.T.; Sharif, R.; Salman, A.; Bashir, M.; Jamil, S. Recent advances in enhanced performance of Ni- rich cathode materials for Li-ion batteries: A review. *Energy Technol*. **2022**, *10*, 2100775, https://doi.org/10.1002/ente.202100775.
28. Jamil, S.; Wang, G.; Fasehullah, M.; Xu, M. Challenges and prospects of nickel-rich layered oxide cathode material. *J. Alloys Compd.* **2022**, *909*, 164727, https://doi.org/10.1016/j.jallcom.2022.164727.

29. Liu, W.; Oh, P.; Liu, X.; Lee, M.-J.; Cho, W.; Chae, S.; Kim, Y.; Cho, J. Nickel-rich layered lithium transition-metal oxide for high-energy lithium-ion batteries. *Angew. Chem. Int. Ed*. **2015**, *54*, 4440–4457, https://doi.org/10.1002/anie.201409262.
30. Yan, W.; Yang, S.; Huang, Y.; Yang, Y.; Yuan, G. A review on doping/coating of nickel-rich cathode materials for lithium- ion batteries. *J. Alloys Compd*. **2020**, *819*, 153048, https://doi.org/10.1016/j.jallcom.2019.153048.
31. Britala, L.; Marinaro, M.; Kucenskis, G. A review of the degradation mechanisms of NCM cathodes and corresponding mitigation strategies. *J. Energy Storage* **2023**, *73A*, 108875, https://doi.org/10.48550/arXiv.2309.07681.
32. Myung, S.T.; Maglia, F.; Park, K.J.; Yoon, C.S.; Lamp, P.; Kim, S.-J.; Sun, Y.-K. Nickel-rich layered cathode materials for automotive lithium-ion batteries: Achievements and perspectives. *ACS Energy Lett*. **2017**, *2*, 196-223, https://doi.org/10.1021/acsenergylett.6b00594.
33. Hou, P.Y.; Yin, J.M.; Ding, M.; Huang, J.; Xu, X. Surface/interfacial structure and chemistry of high-energy nickel-rich layered oxide cathodes: advances and perspectives. *Small* **2017**, *13*, 1701802, https://doi.org/10.1002/smll.201701802.
34. Jung, R.; Metzger, M.; Maglia, F.; Stinner, C.; Gasteiger, H.A. Oxygen release and its effect on the cycling stability of LiNi*x*Mn*y*Co*z*O2(NMC) cathode materials for Li-ion batteries. *J. Electrochem. Soc*. **2017**, *164*, A1361–A1377, https://doi.org/10.1149/2.0021707jes.
35. Strehle, B.; Kleiner, K.; Jung, R.; Chesneau, F.; Mendez, M.; Gasteiger, H.A.; Piana, M. The role of oxygen release from Li- and Mn-rich layered oxides during the first cycles investigated by on-line electrochemical mass spectrometry. *J. Electrochem. Soc*. **2017**, *164*, A400–A406, https://doi.org/10.1149/2.1001702jes.
36. Luo, Y.-H.; Pan, Q.-L.; Wei, H.-X.; Huang, Y.-D.; Tang, L.-B.; Wang, Z.-Y.; He, Z.-J.; Yan, C.; Mao, J.; Dai, K.-H.; Zhang, X.; Zheng, J. Towards Ni-rich layered oxides cathodes with low Li/Ni intermixing by mild molten-salt ion exchange for lithium-ion batteries. *Nano Energy* **2022**, *102*, 107626, https://doi.org/10.1016/j.nanoen.2022.107626.
37. Xiao, P.; Li, W.-H.; Chen, S.; Li, G.; Dai, Z.-J.; Feng, M.-D.; Chen, X.; Yang, W.-S. Effects of Oxygen pressurization on Li^+/Ni^{2+} cation mixing and the oxygen vacancies of $LiNi_{0.8}Co_{0.15}Al_{0.05}O_2$ cathode materials. *ACS Appl. Mater. Interfaces* **2022**, *14*, 31851–31861, https://doi.org/10.1021/acsami.2c05136.
38. Chen, J.-N.; Yang, Y.; Tang, Y.-S.; Wang, Y.-F.; Li, H.; Xiao, X.-H.; Wang, S.-N.; Mariyam, S.D.D.; Etter, M.; Missyul, A.; Tayal, A.; Knapp, M.; Ehrenberg, H.; Indris, S.; Hua, W. Constructing a thin disordered self-protective layer on the LiNiO2 primary particles against oxygen release. *Adv. Funct. Mater*. **2022**, *33*, 2211515, https://doi.org/10.1002/adfm.202211515.
39. Li, X.-H.; Wang, Q.; Guo, H.-Y.; Artrith, N.; Urban, A. Understanding the onset of surface degradation in LiNiO2 cathodes. *ACS Appl. Energy Mater*. **2022**, *5*, 5730–5741, https://doi.org/10.1021/acsaem.2c00012.
40. Duan, Y.; Chen, S.P.; Zhang, L.; Guo, L.; Shi, F.N. Review on oxygen release mechanism and modification strategy of nickel- rich NCM cathode materials for lithium-ion batteries: recent advances and future directions. *Energy Fuel* **2024**, *38*, 5607–5631, https://doi.org/10.1021/acs.energyfuels.3c04636.
41. Buchberger, I.; Seidlmayer, S.; Pokharel, A.; Piana, M.; Hattendorff, J.; Kudejova, P.; Gilles, R.; Gasteiger, H.A. Aging analysis of graphite/$LiNi_{1/3}Mn_{1/3}Co_{1/3}O_2$ cells using XRD, PGAA, and AC impedance. *J. Electrochem. Soc*. **2015**, *162*, A2737–A2746, https://doi.org/10.1149/2.0721514jes.
42. Komagata, S.; Itou, Y.; Kondo, H. Impact of surface layer formation during cycling on the thermal stability of the LiNi0.8Co0.1Mn0.1O2 cathode. *ACS Appl. Mater. Interfaces* **2022**, *14*, 8931–8937, https://doi.org/10.1021/acsami.1c20643.
43. Chen, S.; Zhang, P.; Zhou, X.; Wu, W.; Liu, X.; Liu, Y.; Feng, G.; Zhang, B.; Xing, W.; Zuo, M.; Zhang, P.; Lv, G.; Xiao, Y.; Dou, S.; Xiang, W. Slightly Li-enriched chemistry enabling super stable LiNi0.5Mn0.5O2 cathodes under extreme conditions. *Chem. Sci.* **2024**, *15*, 14415–14424. https://doi.org/10.1039/d4sc03805c.
44. Deng, Z.; Liu, Y.; Wang, L.; Fu, N.; Li, Y.; Luo, Y.; Wang, J.; Xiao, X.; Wang, X.; Yang, X.; He, X.; Zhang, H. Challenges of thermal stability of high-energy layered oxide cathode materials for lithium-ion batteries: a review. *Mater. Today* **2023**, *69*, 236–261 https://doi.org/10.1016/j.mattod.2023.07.024.
45. Liu, K.; Liu, Y.; Lin, D.; Pei, A.; Cui, Y. Materials for lithium-ion battery safety. *Sci. Adv*. **2018**, *4*, eaas9820, https://doi.org/10.1126/sciadv.aas9820.
46. Jin, Y.; Zheng, Z.; Wei, D.; Jiang, X.; Lu, H.; Sun, L.; Tao, F.; Guo, D.; Liu, Y.; Gao, J. Detection of micro-scale Li dendrite via H2 gas capture for early safety warning. *Joule* **2020**, *4*, 1714-1729, https://doi.org/10.1016/j.joule.2020.05.016.

47. Liao, Z.H.; Zhang, S.; Li, K.; Zhang, G.Q.; Habetler, T.G. A survey of methods for monitoring and detecting thermal runaway of lithium-ion batteries. *J. Power Sources* **2019**, *436*, 226879, https://doi.org/10.1016/j.jpowsour.2019.226879.
48. Guo, X.; Guo, S.; Wu, C.; Li, J.; Liu, C.; Chen, W. Intelligent Monitoring for Safety-Enhanced Lithium-Ion/Sodium-Ion Batteries. *Adv. Energy Mater.* **2023**, *13*, 2203903, https://doi.org/10.1002/aenm.202203903.
49. Kaur, P.; Bagchi, S.; Gribble, D.; Pol, V.G.; Bhondekar, A.P. Impedimetric Chemosensing of Volatile Organic Compounds Released from Li-Ion Batteries. *ACS Sens.* **2022**, *7*, 674–683, https://doi.org/10.1021/acssensors.2c00113.
50. Cai, T.; Valecha, P.; Tran, V.; Engle, B.; Stefanopoulou, A.; Siegel, J. Detection of Li-ion battery failure and venting with Carbon Dioxide sensors. *Etransportation* **2021**, *7*, 100100. https://doi.org/10.1016/j.etran.2020.100100.
51. Santos-Carballal, D.; Lupan, O.; Magariu, N.; Ababii, N.; Kruger, H.; Bodduluri, M.T.; de Leeuw, N.H.; Hansen, S.; Adelung, R. Al_2O_3/ZnO composite-based sensors for battery safety applications: An experimental and theoretical investigation. *Nano Energy* **2023**, *109*, 108301, https://doi.org/10.1016/j.nanoen.2023.108301.
52. Essl, C.; Seifert, L.; Rabe, M.; Fuchs, A. Early detection of failing automotive batteries using gas sensors. *Batteries* **2021**, *7*, 25, https://doi.org/10.3390/batteries7020025.
53. Mateev, V.; Marinova, I.; Kartunov, Z. Gas Leakage Source Detection for Li-Ion Batteries by Distributed Sensor Array. *Sensors* **2019**, *19*, 2900, https://doi.org/10.3390/s19132900.
54. Shi, S.; Lyu, N.; Jiang, X.; Song, Y.; Lu, H.; Jin, Y. Hydrogen gas diffusion behavior and detector installation optimization of lithium ion battery energy-storage cabin. *J. Energy Storage* **2023**, *67*, 107510, https://doi.org/10.1016/j.est.2023.107510.
55. Li, B.; Lai, P.T.; Tang, W.M. Influence of Source/Drain Catalytic Metal and Fabrication Method on OTFT-Based Hydrogen Sensor. *IEEE Trans. Electron. Devices* **2022**, *69*, 2038–2042, https://doi.org/10.1109/TED.2022.3151044.
56. Ghosh, S.; Rajan, L.; Varghese, A. Junctionfree Gate Stacked Vertical TFET Hydrogen Sensor at Room Temperature. *IEEE Trans. Nanotechnol.* **2022**, *21*, 655–662, https://doi.org/10.1109/TNANO.2022.3217652.
57. Zhou, S.; Xiao, M.; Liu, F.; He, J.; Lin, Y.; Zhang, Z. Sub-10 parts per billion detection of hydrogen with floating gate transistors built on semiconducting carbon nanotube film. *Carbon* **2021**, *180*, 41–47, https://doi.org/10.1016/j.carbon.2021.04.076.
58. Skucha, K.; Fan, Z.Y.; Jeon, K.; Javey, A.; Boser, B. Palladium/silicon nanowire Schottky barrier-based hydrogen sensors. *Sens. Actuators B Chem.* **2010**, *145*, 232–238, https://doi.org/10.1016/j.snb.2009.11.067.
59. Mollaamin, F. Competitive Intracellular Hydrogen-Nanocarrier Among Aluminum, Carbon, or Silicon Implantation: a Novel Technology of Eco-Friendly Energy Storage using Research Density Functional Theory. *Russ. J. Phys. Chem. B* **2024**, *18*, 805–820, https://doi.org/10.1134/S1990793124700131.
60. Jang, S.; Jung, S.; Baik, K.H. Hydrogen sensing performance of ZnO Schottky diodes in humid ambient conditions with PMMA membrane layer. *Sensors* **2020**, *20*, 835, https://doi.org/10.3390/s20030835.
61. Ghosh, S.; Rajan, L. Room Temperature Hydrogen Sensing Investigation of Zinc Oxide Schottky Thin-Film Transistors: Dependence on Film Thickness. *IEEE Trans. Electron. Devices* **2020**, *67*, 5701–5709, https://doi.org/10.1109/TED.2020.3032084.
62. Ratan, S.; Kumar, C.; Kumar, A.; Jarwal, D.K.; Mishra, A.K.; Upadhyay, R.K.; Singh, A.P.; Jit, S. Room temperature high hydrogen gas response in Pd/TiO_2/Si/Al capacitive sensor. *Micro Nano Lett.* **2020**, *15*, 632–635, https://doi.org/10.1049/mnl.2020.0154.
63. Constantinoiu, I.; Viespe, C. Development of Pd/TiO_2 Porous Layers by Pulsed Laser Deposition for Surface Acoustic Wave H_2 Gas Sensor. *Nanomaterials* **2020**, *10*, 760, https://doi.org/10.3390/nano10040760.
64. Hosoki, A.; Nishiyama, M.; Sakurai, N.; Igawa, H.; Watanabe, K. Long-Term Hydrogen Detection Using a Hetero-Core Optical Fiber Structure Featuring Au/Ta_2O_5/Pd/Pt Multilayer Films. *IEEE Sens. J.* **2020**, *20*, 227–233, https://doi.org/10.1109/JSEN.2019.2942599.
65. Dai, J.; Li, Y.; Ruan, H.; Ye, Z.; Chai, N.; Wang, X.; Qiu, S.; Bai, W.; Yang, M. Fiber Optical Hydrogen Sensor Based on WO3-Pd2Pt-Pt Nanocomposite Films. *Nanomaterials* **2021**, *11*, 128, https://doi.org/10.3390/nano11010128.
66. Koo, W.T.; Cho, H.J.; Kim, D.H.; Kim, Y.H.; Shin, H.; Penner, R.M.; Kim, I.D. Chemiresistive Hydrogen Sensors: Fundamentals, Recent Advances, and Challenges. *ACS Nano* **2020**, *14*, 14284–14322, https://doi.org/10.1021/acsnano.0c05307.

67. Favier, F.; Walter, E.C.; Zach, M.P.; Benter, T.; Penner, R.M. Hydrogen sensors and switches from electrodeposited palladium mesowire arrays. *Science* **2001**, *293*, 2227–2231, https://doi.org/10.1126/science.1063189.
68. Zhou, L.; Li, Z.; Chang, X.; Liu, X.; Hu, Y.; Li, M.; Xu, P.; Pinna, N.; Zhang, J. PdRh-Sensitized Iron Oxide Ultrathin Film Sensors and Mechanistic Investigation by Operando TEM and DFT Calculation. *Small* **2023**, *19*, 2301485, https://doi.org/10.1002/smll.202301485.
69. Ahmad, W.; Yan, W.; Ling, M.; Liang, C. DNA-Incorporated Biomimetic Olfactory Neuroepithelium That Facilitates Artificial Intelligence. *Adv. Intell. Syst.* **2023**, *5*, 2200396, https://doi.org/10.1002/aisy.202200396.
70. Zhu, J.; Cho, M.; Li, Y.; He, T.; Ahn, J.; Park, J.; Ren, T.-L.; Lee, C.; Park, I. Machine learning-enabled textile-based graphene gas sensing with energy harvesting-assisted IoT application. *Nano Energy* **2021**, *86*, 106035, https://doi.org/10.1016/j.nanoen.2021.106035.
71. Kumar, A.; Zhao, Y.; Abraham, S.R.; Thundat, T.; Swihart, M.T. Pd Alloy Nanosheet Inks for Inkjet-Printable H2 Sensors on Paper. *Adv. Mater. Interfaces* **2022**, *9*, 2200363, https://doi.org/10.1002/admi.202200363.
72. Yang, S.; Li, Q.; Li, C.; Cao, T.; Wang, T.; Fan, F.; Zhang, X.; Fu, Y. Enhancing the Hydrogen-Sensing Performance of p-Type PdO by Modulating the Conduction Model. *ACS Appl. Mater. Interfaces* **2021**, *13*, 52754–52764, https://doi.org/10.1021/acsami.1c13034.
73. Jeon, J.-Y.; Park, S.-J.; Ha, T.-J. Functionalization of Zinc Oxide Nanoflowers with Palladium Nanoparticles via Microwave Absorption for Room Temperature-Operating Hydrogen Gas Sensors in the ppb Level. *ACS Appl. Mater. Interfaces* **2021**, *13*, 25082–25091, https://doi.org/10.1021/acsami.1c03283.
74. Monajjemi, M.; Mollaamin, F.; Shahriari, S.; Khlaj, Z.; Sakhaeinia, H.; Alihosseini, A. Interaction of Nano-Boron Nitride Sheets with Electrodes in Lithium Ion Battery for Increasing Voltage and Amperage. *Russ. J. Phys. Chem. B* **2024**, *18*, 1090–1112, https://doi.org/10.1134/S1990793124700465.
75. Monajjemi, M.; Mohammadi, S.; Shahriari, S.; Mollaamin, F. Experimental and Theoretical Studies of ZnO Nanotubes: an Approach to Chemical Physics Characterization of ZnONTs, Including Morphology, Piezoelectric, and Density of States. *Russ. J. Phys. Chem. B* **2024**, *18*, 308–324, https://doi.org/10.1134/S1990793124010342.
76. Shahriari, S.; Soofi, N.S.; Farzi, F.; Attarikhasraghi, N.; Khosravi, S.; Babaei Tuskiee, B.B.; Esmkhani, R.; Monajjemi, M. Interaction of nano-boron nitride/graphene sheets with anode lithium ion battery. *J. Comput. Theor. Nanosci.* **2016**, *13*, 3070-3082, https://doi.org/10.1166/JCTN.2016.4959.
77. Mollaamin, F.; Monajjemi, M. Nanomaterials for Sustainable Energy in Hydrogen-Fuel Cell: Functionalization and Characterization of Carbon Nano-Semiconductors with Silicon, Germanium, Tin or Lead through Density Functional Theory Study. *Russ. J. Phys. Chem. B* **2024**, *18*, 607–623, https://doi.org/10.1134/S1990793124020271.
78. Mollaamin, F.; Shahriari, S.; Monajjemi, M. Influence of Transition Metals for Emergence of Energy Storage in Fuel Cells through Hydrogen Adsorption on the MgAl Surface. *Russ. J. Phys. Chem. B* **2024**, *18*, 398–418, https://doi.org/10.1134/S199079312402026X.
79. Mollaamin, F.; Monajjemi, M. Tailoring and functionalizing the graphitic-like GaN and GaP nanostructures as selective sensors for NO, NO_2, and NH_3 adsorbing: a DFT study. *J. Mol. Model.* **2023**, *29*, 170, https://doi.org/10.1007/s00894-023-05567-8.
80. Mollaamin, F.; Monajjemi, M. Molecular modelling framework of metal-organic clusters for conserving surfaces: Langmuir sorption through the TD-DFT/ONIOM approach. *Mol. Simul.* **2023**, *49*, 365–376, https://doi.org/10.1080/08927022.2022.2159996.
81. Monajjemi, M.; Razavian, M.H.; Mollaamin, F.; Naderi, F.; Honarparvar, B.A. A theoretical thermochemical study of solute-solvent dielectric effects in the displacement of codon-anticodon base pairs. *Russ. J. Phys. Chem. A* **2008**, *82*, 2277–2285, https://doi.org/10.1134/S0036024408130207.
82. Mollaamin, F. Anchoring of 2D layered materials of $Ge_5Si_5O_{20}$ for (Li/Na/K)-(Rb/Cs) batteries towards Eco-friendly energy storage. *BMC Chem.* **2025**, *19*, 233, https://doi.org/10.1186/s13065-025-01593-0.
83. Goodenough, J.B.; and Kim, Y. Challenges for rechargeable Li batteries. *Chem. Mater.* **2010**, *22*, 587–603, https://doi.org/10.1021/cm901452z.
84. Feng, X.; Fang, M.; He, X.; Ouyang, M.; Lu, L.; Wang, H.; and Zhang, M. Thermal runaway features of large format prismatic lithium ion battery using extended volume accelerating rate calorimetry. *J. Power Sources* 2014, *255*, 294–301, https://doi.org/10.1016/j.jpowsour.2014.01.005.

85. Basu, S.; Hariharan, K.S.; Kolake, S.M.; Song, T.; Sohn, D.K.; and Yeo, T. Coupled electrochemical thermal modelling of a novel Li-ion battery pack thermal management system. *Appl. Energy* **2016**, *181*, 1–13, https://doi.org/10.1016/j.apenergy.2016.08.049.
86. Wang, Q.; Ping, P.; Zhao, X.; Chu, G.; Sun, J.; and Chen, C. Thermal runaway caused fire and explosion of lithium ion battery. *J. Power Sources* **2012**, *208*, 210–224, https://doi.org/10.1016/j.jpowsour.2012.02.038.
87. Lu, L.; Han, X.; Li, J.; Hua, J.; and Ouyang, M. A review on the key issues for lithium-ion battery management in electric vehicles. *J. Power Sources* **2013**, *226*, 272–288, https://doi.org/10.1016/j.jpowsour.2012.10.060.
88. Rahimi-Eichi, H.; Ojha, U.; Baronti, F.; and Chow, M.Y. Battery management system an overview of its application in the smart grid and electric vehicles. *IEEE Ind. Electron. Mag.* **2013**, *7*, 4–16, https://doi.org/10.1109/MIE.2013.2250351.
89. Hong, J.; Wang, Z.; and Yao, Y. Fault prognosis of battery system based on accurate voltage abnormity prognosis using long shortterm memory neural networks. *Appl. Energy* **2019**, *251*, 113381, https://doi.org/10.1016/j.apenergy.2019.113381.
90. Mollaamin, F.; Monajjemi, M. Graphene-based resistant sensor decorated with Mn, Co, Cu for nitric oxide detection: Langmuir adsorption & DFT method. *Sensor Rev.* **2023**, *43*, 266–279, https://doi.org/10.1108/SR-03-2023-0040.
91. Grandjean, T.R.; Barai, A.; Hosseinzadeh, E.; Guo, Y.; Mcgordon, A.; and Marco, J. Large format lithium ion pouch cell full thermal characterisation for improved electric vehicle thermal management. *J. Power Sources* **2017**, *359*, 215–225, https://doi.org/10.1016/j.jpowsour.2017.05.016.
92. Seong, W.M.; Cho, K.H.; Park, J.W.; Park, H.; Eum, D.; Lee, M.H.; Kim, I.S.; Lim, J.; Kang, K. Controlling residual lithium in high-nickel (>90 %) lithium layered oxides for cathodes in lithium-ion batteries. *Angew. Chem. Int. Ed.* **2020**, *59*, 18662–18669, https://doi.org/10.1002/anie.202007436.
93. Li, L.; Chen, J.; Huang, H.; Tan, L.; Song, L.; Wu, H.H.; Wang, C.; Zhao, Z.; Yi, H.; Duan, J.; Dong, T. Role of residual Li and oxygen vacancies in Ni-rich cathode materials. *ACS Appl. Mater. Interfaces* **2021**, *13*, 42554–42563, https://doi.org/10.1021/acsami.1c06550.
94. Klein, S.; Bärmann, P.; Fromm, O.; Borzutzki, K.; Reiter, J.; Fan, Q.; Winter, M.; Placke, T.; Kasnatscheew, J. Prospects and limitations of single-crystal cathode materials to overcome cross-talk phenomena in high-voltage lithium ion cells. *J. Mater. Chem. A* **2021**, *9*, 7546–7555, https://doi.org/10.1039/D0TA11775G.
95. Hou, X.; Liu, X.; Wang, H.; Zhang, X.; Zhou, J.; Wang, M. Specific countermeasures to intrinsic capacity decline issues and future direction of $LiMn_2O_4$ cathode. *Energy Storage Mater.* **2023**, *57*, 577–606, https://doi.org/10.1016/j.ensm.2023.02.015.
96. Wang, B.; Zhang, F.-L.; Zhou, X.A.; Wang, P.; Wang, J.; Ding, H.; Dong, H.; Liang, W.B.; Zhang, N.S.; Li, S.Y. Which of the 4598nickel-rich NCM and NCA is structurally superior as a cathode material for lithium-ion batteries?. *J. Mater. Chem. A* **2021**, *9*, 13540–13551, https://doi.org/10.1039/D1TA01128F.
97. Wang, Z.; Yuan, J.; Zhu, X.; Wang, H.; Huang, L.; Wang, Y.; Xu, S. Overcharge-to-thermal-runaway behavior and safety assessment of commercial lithium-ion cells with different cathode materials: A comparison study. *J. Energy Chem.* **2021**, *55*, 484-498, https://doi.org/10.1016/j.jechem.2020.07.028.
98. Xiong, D.J.; Hynes, T.; Ellis, L.D.; Dahn, J.R. Effects of surface coating on gas evolution and impedance growth at LiNixMnyCo1−x−yO2 Positive electrodes in Li-ion cells. *J. Electrochem. Soc.* **2017**, *164*, A3174-A3181, https://doi.org/10.1149/2.0991713jes.
99. Wang, X.X.; Ding, Y.L.; Deng, Y.P.; Chen, Z.W. Ni-rich/Co-poor layered cathode for automotive Li-ion batteries: Promises and challenges. *Adv. Energy Mater.* **2020**, *10*, 1903864, https://doi.org/10.1002/aenm.201903864.
100. Xu, H.; Li, Z.; Liu, T.; Han, C.; Guo, C.; Zhao, H.; Li, Q.; Lu, J.; Amine, K.; Qiu, X.; Impacts of dissolved Ni2+ on the solid electrolyte interphase on a graphite anode. *Angew. Chem. Int. Ed.* **2022**, *61*, e202202894, https://doi.org/10.1002/anie.202202894.
101. Huang, Y.; Ji, Y.; Zheng, G.; Cao, H.; Xue, H.; Yao, X.; Wang, L.; Chen, S.; Yin, Z.; Pan, F.; Yang, L. Tailored Interphases Construction for Enhanced Si Anode and Ni-Rich Cathode Performance in Lithium-Ion Batteries. *Chinese Chem. Soc. Chem.* **2025**, *7*, 429–439, https://doi.org/10.31635/ccschem.024.202404120.
102. Zhang, Y.; Zhang, Y.; Wang, X.; Gong, H.; Cao, Y.; Ma, K.; Zhang, S.; Wang, S.; Yang, W.; Wang, L.; Sun, J. Trace multifunctional additive enhancing 4.8 V ultra-high voltage performance of Ni-rich cathode and SiOx anode battery. *Adv. Energy Mater.* **2025**, *15*, 2403751. https://doi.org/10.1002/aenm.202403751.

103. Li, L.; Min, X.; Monajjemi, M. A novel cathode material synthesis and thermal characterization of (1-xy) LiCo1/3Ti1/3Fe1/3PO4, xLi2MnPO4, yLiFePO4 composites for lithium-ion batteries (LIBs). *Molecules* **2022**, *27*, 8486, https://doi.org/10.3390/molecules27238486.
104. Shboul, A.A.; Shih, A.; Oukachmih, M.; Izquierdo, R. ppb Sensing Level Hydrogen Sulphide at Room Temperature Using Indium Oxide Gas Sensors. In Proceedings of the 2019 IEEE SENSORS, Montreal, QC, Canada, 27-30 Oct. 2019; 2019 IEEE SENSORS, **2019**; pp. 1-4, https://doi.org/10.1109/SENSORS43011.2019.8956528.
105. Saqib, N.; Ganim, C.M.; Shelton, A.E.; Porter, J.M. On the decomposition of carbonate-based lithium-ion battery electrolytes studied using operando infrared spectroscopy. *J. Electrochem. Soc.* **2018**, *165*, A4051, https://doi.org/10.1149/2.1051816jes.
106. Liu, Z.; He, H. Model-based Sensor Fault Diagnosis of a Lithium-ion Battery in Electric Vehicles. *Energies* **2015**, *8*, 6509–6527, https://doi.org/10.3390/en8076509.
107. Wu, C.; Zhu, C.; Ge, Y.; Zhao, Y. A Review on Fault Mechanism and Diagnosis Approach for Li-Ion Batteries. *J. Nanomater.* **2015**, *2015*, 631263, https://doi.org/10.1155/2015/631263.
108. Dubarry, M.; Berecibar, M.; Devie, A.; Anseán, D.; Omar, N.; Villarreal, I. State of health battery estimator enabling degradation diagnosis: Model and algorithm description. *J. Power Sources* **2017**, *360*, 59–69, https://doi.org/10.1016/j.jpowsour.2017.05.121.
109. Dey, S.; Mohon, S.; Pisu, P.; Ayalew, B. Sensor Fault Detection, Isolation, and Estimation in Lithium-Ion Batteries. *IEEE Trans. Control Syst. Technol.* **2016**, *24*, 2141–2149, https://doi.org/10.1109/TCST.2016.2538200.
110. Lelie, M.; Braun, T.; Knips, M.; Nordmann, H.; Ringbeck, F.; Zappen, H.; Sauer, D. Battery Management System Hardware Concepts: An Overview. *Appl. Sci.* **2018**, *8*, 534, https://doi.org/10.3390/app8040534.

Publisher's Note & Disclaimer